Supporting information for: Molecular Seesaw: How Increased Hydrogen Bonding Can Hinder Excited-State Proton Transfer

Ralph Welsch,[*,†] Eric Driscoll,[*,‡] Jahan M. Dawlaty,[*,‡] and Thomas F. Miller III[*,†]

†*Division of Chemistry and Chemical Engineering, California Institute of Technology, 1200 E. California Blvd., Pasadena, CA 91125, USA*

‡*Department of Chemistry, University of Southern California, Los Angeles, CA 90089-1062, United States*

E-mail: rwelsch@caltech.edu; edriscol@usc.edu; dawlaty@usc.edu; tfm@caltech.edu

I. Experimental methods

a. Materials

1,3-bis(2-pyridylimino)-4,7-dihydroxyisoindole (diol) and 1,3-bis(2-pyridylimino)-4-ethoxy-7-hydroxyisoindole (ethoxy-ol) were synthesized previously by Hanson.[S1] To prepared the deuterated samples (diol-d and ethoxy-ol-d) the hydroxylic protons were exchanged for deuterons by dissolving and recrystallizing each compound in CH_3OD (Sigma-Aldrich).

b. Transient Absorption

Spectroscopic grade acetonitrile solutions of each compound were made with ∼0.3 OD in a 100 μm path length fused silica flow cell. The concentration for each solution was ∼2 mM.

The transient absorption apparatus has been described previously,[S2] with modifications noted here. Briefly, the fundamental of a Ti:sapphire chirped pulse amplifier was frequency doubled in type II BBO to produce a pump pulse with center wavelength 393 nm. The pump was attenuated to 300 nJ with neutral density filters. Approximately 100 nJ of the fundamental was focused into a 2 mm path length cuvet filled with DI water to generate a white light continuum probe pulse. The probe was split into two arms, reference and sample, in a balanced detection scheme. The sample arm is sent to a motion controlled retro reflector and is focused to the same spot on the sample as the pump. The reference arm has fixed path length and passes through a point on the sample that is never pumped. The spectra of both the sample and reference probes are detected with a grating spectrometer and 100x1340 element CCD array. The balanced transient absorption is then calculated via the expression $\Delta A_{balanced} = \Delta A_{sample} - \Delta A_{reference} = \log \frac{I_{s,u} * I_{r,p}}{I_{s,p} * I_{r,u}}$, where I is intensity and s, r, p and u stand for sample, reference, pumped, and unpumped. In this scheme any shot to shot fluctuations in the intensity of the probe are captured in $\Delta A_{reference}$ and removed from the real transient absorption that is induced by the pump. The time resolution of the system was measured by cross correlating the pump and probe using the solvent response (Fig. S1).

The system resolution is taken to be the time difference between the half minimum and half maximum of this response, measured to be 235 fs.

The TA data was cropped at approximately 300 fs to exclude any dynamics associated with the coherent spike. Singular value decomposition (SVD)[S3] was used to determine the number of transient species. The selection criterion for a significant component was that it's singular value must be greater than 2% of the first singular value. In all cases, the data was well described by two components. A large amplitude background component (first singular value) which does not decay with time, and a smaller second component which decays on femtosecond time scales. The latter is assigned to the intramolecular proton transfer events on the basis that the growth of the stimulated emission peaks in the transient spectra roughly match the steady state emission peaks ($\lambda \approx 595nm$).[S2] Each transient was well described by a single exponential function, with the time constants reported in Table S1.

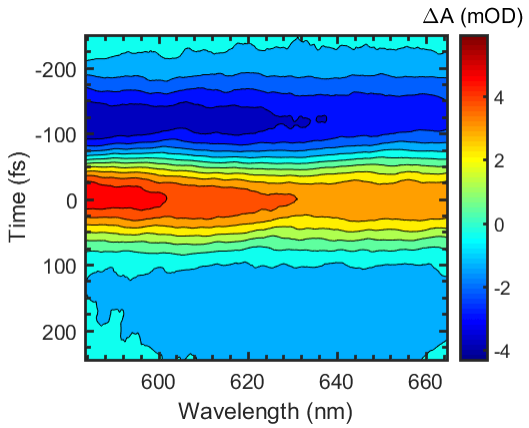

Figure S1: The coherent spike due to the interaction between the pump and probe in pure acetonitrile and the sample holder.

Table S1: Proton transfer time constants measured in acetonitrile. For comparison transfer times from Ref. S2 measured in other solvents are given.

Time constants (fs)				
Solvent	diol	diol-D	ethoxy-ol	ethoxy-ol-D
acetonitrile	319	583	257	235
methanol	710	N/A	427	N/A
chloroform	530	-	-	-
cyclohexane	1230	-	-	-

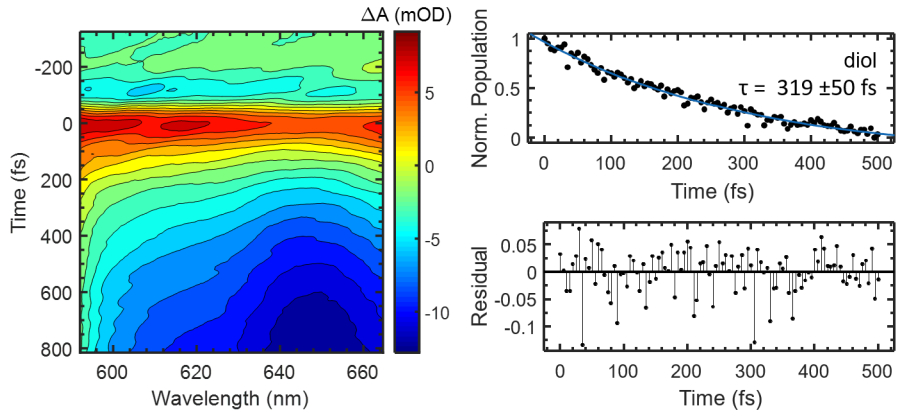

Figure S2: Transient absorption of the diol in acetonitrile. (left) Single exponential fit of the population dynamics retrieved by SVD. (right)

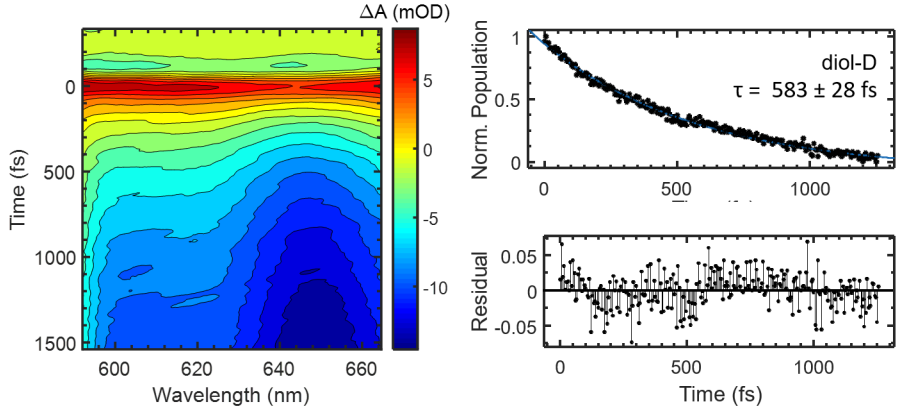

Figure S3: Transient absorption of the diol-D in acetonitrile. (left) Single exponential fit of the population dynamics retrieved by SVD. (right)

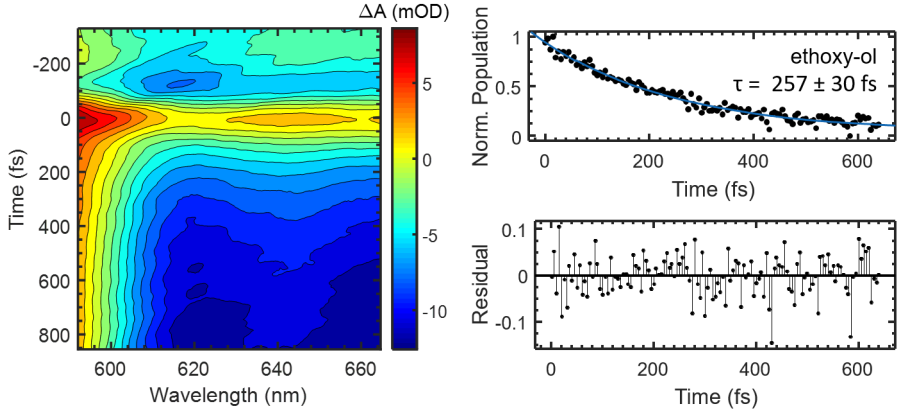

Figure S4: Transient absorption of the ethoxy-ol in acetonitrile. (left) Single exponential fit of the population dynamics retrieved by SVD. (right)

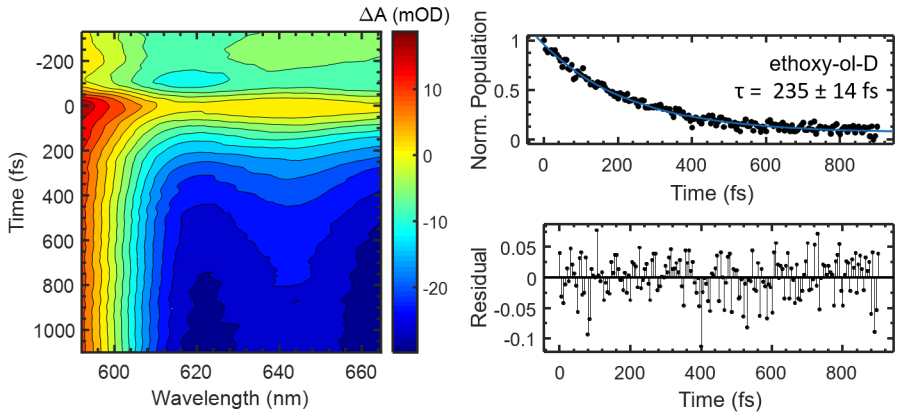

Figure S5: Transient absorption of the ethoxy-ol-D in acetonitrile. (left) Single exponential fit of the population dynamics retrieved by SVD. (right)

II. Computational methods

a. Thermal rate constant calculations

Thermal rate constants are calculated using a separable, semi-classical transition state theory:[S4]

$$k(T) = \kappa\ \sigma\ \frac{k_{\mathrm{B}}T}{h}\frac{1}{Q^{\mathrm{r}}_{\mathrm{vib},1}}\prod_{i=2}^{F}\frac{Q^{\ddagger}_{\mathrm{vib},i}}{Q^{\mathrm{r}}_{\mathrm{vib},i}}\mathrm{e}^{-\beta\Delta V}. \tag{1}$$

Here $\beta = \frac{1}{k_{\mathrm{B}}T}$, σ is the symmetry number (i.e. one for the ethoxy-ol and two for the diol), $Q^{\mathrm{r}}_{\mathrm{vib},i}$ denotes the harmonic vibrational partition function of the i-th normal mode at the reactant minimum, $Q^{\ddagger}_{\mathrm{vib},i}$ denotes the harmonic vibrational partition function of the i-th normal mode at the transition state, and the normal modes are sorted such that the reaction coordinate (i.e. OH stretching mode at the minimum, unstable mode at the transition state) comes first. ΔV is the potential energy difference between the reactants and the transition state and κ denotes a tunneling correction factor:

$$\kappa = \frac{\mathrm{e}^{\beta\Delta E}}{1+\mathrm{e}^{2\pi\Delta E/|\omega_{\mathrm{I}}|}} + \frac{1}{2}\int_{-\infty}^{\pi\Delta E/|\omega_{\mathrm{I}}|}\mathrm{d}\theta\ \mathrm{e}^{\beta|\omega_{\mathrm{I}}|\theta/\pi}\ \mathrm{sech}^2\left(\theta\right), \tag{2}$$

where ΔE is the zero-point energy corrected barrier height, defined as $\Delta E = \Delta V + E^{\ddagger}_{\mathrm{ZP}} - E^{\mathrm{r}}_{\mathrm{ZP}}$, $E^{\ddagger}_{\mathrm{ZP}}$ and $E^{\mathrm{r}}_{\mathrm{ZP}}$ are the harmonic zero-point energies at the transition state and the reactant minimum, respectively, and $\omega_{\mathrm{I}} = \omega^{\ddagger}_{\mathrm{vib},1}$ is the frequency of the unstable mode at the transition state. This tunneling correction factor is closely related to the Wigner tunneling correction factor, except that it performs better at temperatures close to and below the crossover temperature as it derived using a truncated parabolic barrier instead of an infinite parabolic barrier.

One of the assumptions made in this model is that the proton transfer can be described using a separable, one-dimensional reaction coordinate. To test if this assumption is justified, we investigate the expansion of the unstable normal mode at the transition state in terms of the reactant normal modes:

$$c_i = \left\langle \omega^{\ddagger}_{\mathrm{vib},1} \middle| \omega^{\mathrm{r}}_{\mathrm{vib},i} \right\rangle, \tag{3}$$

where $\left|\omega^{\ddagger}_{\mathrm{vib},1}\right\rangle$ is the unstable normal mode at the transition state and $\left|\omega^{\mathrm{r}}_{\mathrm{vib},i}\right\rangle$ are the reactant normal modes. The largest expansion factors c_i for the ethoxy-ol using B3LYP/6-31++G(d) are shown in Tab. S2. The results clearly show that the largest component is along the OH stretch of the reactant minimum and that no other reactant normal mode has a major contribution. This validates using the separable model.

Table S2: Expansion coefficients for the instable normal mode at the transition state in terms of the reactant minimum normal modes as defined in Eq. 3 for the ethoxy-ol. Mode 1 is the OH stretch.

Mode	c_i^2
1	0.83
89	0.02
14	0.02
28	0.02
25	0.01
⋮	⋮

The same analysis for the diol is presented in Tab. S3. Due to the symmetry of the

molecule and the two OH groups, there are two normal modes with significant contributions, namely, the asymmetric (mode 1) and symmetric (mode 102) OH stretching modes. However, the two normal modes can be linearly combined to two local modes describing the OH stretching motion of the proton to be transferred and of the other proton as $|\Psi_{\mathrm{local}}\rangle = \frac{1}{\sqrt{2}}|\omega_1^r\rangle \pm \frac{1}{\sqrt{2}}|\omega_{107}^{\mathrm{r}}\rangle$. As both normal modes have very similar frequencies (asymmetric stretch: 3188 cm^{-1}, symmetric stretch: 3202 cm^{-1}), the local modes are likewise close in frequency. Projecting the instable normal mode onto these two local modes gives squared expansion coefficients of 0.85 (for the negative admixture) and < 0.01 (for the positive admixture). Thus, the use of the separable approach is again found to be justified.

Table S3: Expansion coefficients for the instable normal mode at the transition state in terms of the reactant minimum normal modes as defined in Eq. 3 for the diol. Mode 1 is the asymmetric OH stretch and mode 102 is the symmetric OH stretch.

Mode	c_i^2
1	0.43
102	0.42
19	0.02
81	0.02
12	0.01
⋮	⋮

b. Electronic structure calculations

All electronic structure calculations are carried out using the Gaussian09 software package.[S5] Ground-state calculations employ density functional theory (DFT), and excited-state calculations employ time-dependent (TD) DFT. Solvation effects are included using a polarizable continuum model (PCM)[S6] with a dielectric constant of $\epsilon = 33$. Minima in the ground and first singlet excited state are calculated using the Berny algorithm.[S7] Transition states were obtained using the Synchronous Transit-Guided Quasi-Newton method[S8,S9] method and linear response PCM. All geometry optimizations were repeated for each combination of exchange-correlation functional and basis set, to ensure the consistency of each stationary-

point geometry and its corresponding energy surface.Throughout all geometry optimizations, we confirmed that the character of the excited state remains the same. Minimum geometries are in all cases confirmed to exhibit no imaginary vibrational frequencies, and transition state geometries are confirmed to exhibit a single imaginary vibrational frequency. Excited-state normal modes are calculated using numerical second derivates. Barrier heights for the reactions (i.e., ΔV in Eqs. 1 and 2) are obtained using a state-specific (SS) PCM,[S10,S11] while geometry optimizations and harmonic frequency calculations employ the standard linear response (LR) PCM.[S6] The SS correction is expected to be more important for the calculation of barrier heights than it would be for the gradients or vibrational frequencies, as barrier heights involve energy differences between geometries that are significantly different.We employ the B3LYP,[S12,S13] CAM-B3LYP,[S14] and M062X[S15] exchange-correlation functionals and the TZVP[S16,S17] and 6-31++G(d)[S18] basis sets.

Table S4: Potential energies in kcal/mol for the lowest- and second-lowest singlet excited states (S_1 and S_2, respectively) relative to the reactant minimum-energy geometry on the S_1 state, calculated using B3LYP/TZVP and a state-specific PCM.

	S_1			S_2		
	Reactants	Transition state	Products	Reactants	Transition state	Products
Ethoxy-ol	0.0	4.3	-3.7	9.0	16.9	11.0
Diol	0.0	5.4	-5.1	6.6	16.5	8.3

The experimentally observed quantum yields and excited-state lifetimes suggest that the ground-state system is photo-excited to a singlet excited state in both molecules.[S1] Thus, this work focuses on the lowest singlet excited state S_1. Excitation from the the ground-state to this excited state is dominated by a HOMO-to-LUMO transition and exhibits a shift in electronic density from the OH group to the opposite N, as can be seen from the plot of the electron-density differences between the ground state and S_1 (Figs. S6 and S7). The charge-transfer character of the excitation can be expected from experiment, as it helps to drive the rapid ESIPT.[S2] Our TD-DFT calculations find that there is also a second low-lying singlet state S_2 present in the Franck-Condon region. This state is dominated by a transition from

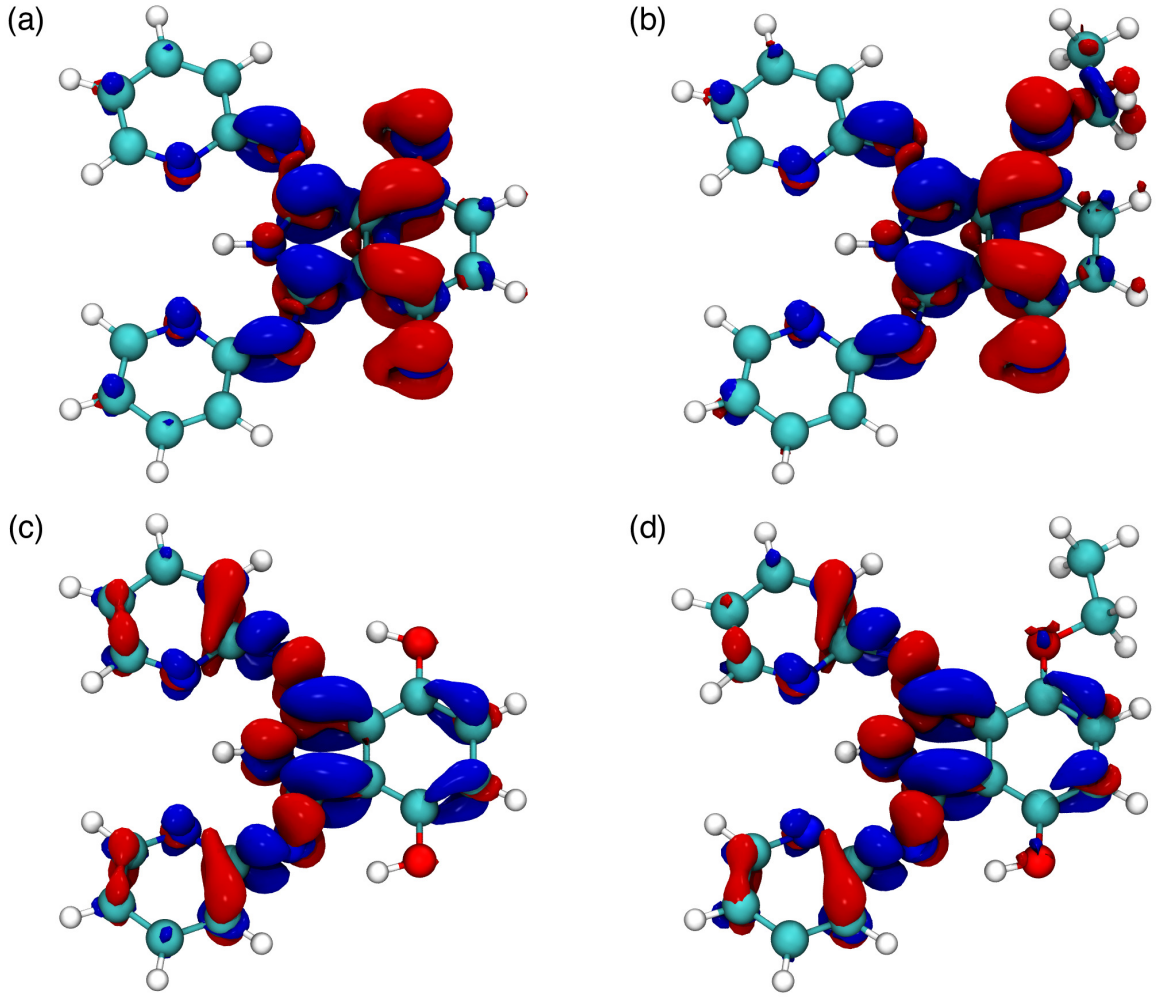

Figure S6: Electron density ρ differences between the ground state S_0 and the first and second excited states S_1 and S_2 at the Franck-Condon point. Positive parts are shown in red and negative parts in blue. (a) Diol, $\rho_{S_0} - \rho_{S_1}$ (b) Ethoxy-ol, $\rho_{S_0} - \rho_{S_1}$ (c) Diol, $\rho_{S_0} - \rho_{S_2}$ (d) Ethoxy-ol, $\rho_{S_0} - \rho_{S_2}$.

the second highest occupied molecular orbital to the LUMO and has a different character than S_1 (see Figs. S6 and S7). The S_2 state is neglected in the present treatment as it has no charge-transfer character and does not create a significant driving force for the ESIPT reaction; for the S_2 potential energy surface Tab. S4 gives the relative energies of the reactant and product species as well as the barrier height calculated using B3LYP/TZVP for both low-lying singlet excited states in the diol and the ethoxy-ol. It should be noted that in comparison to the experiment, an initial excitation to S_2 and ultrafast relaxation to S_1 on a timescale faster than the instrumental limitations can not be completely excluded; however,

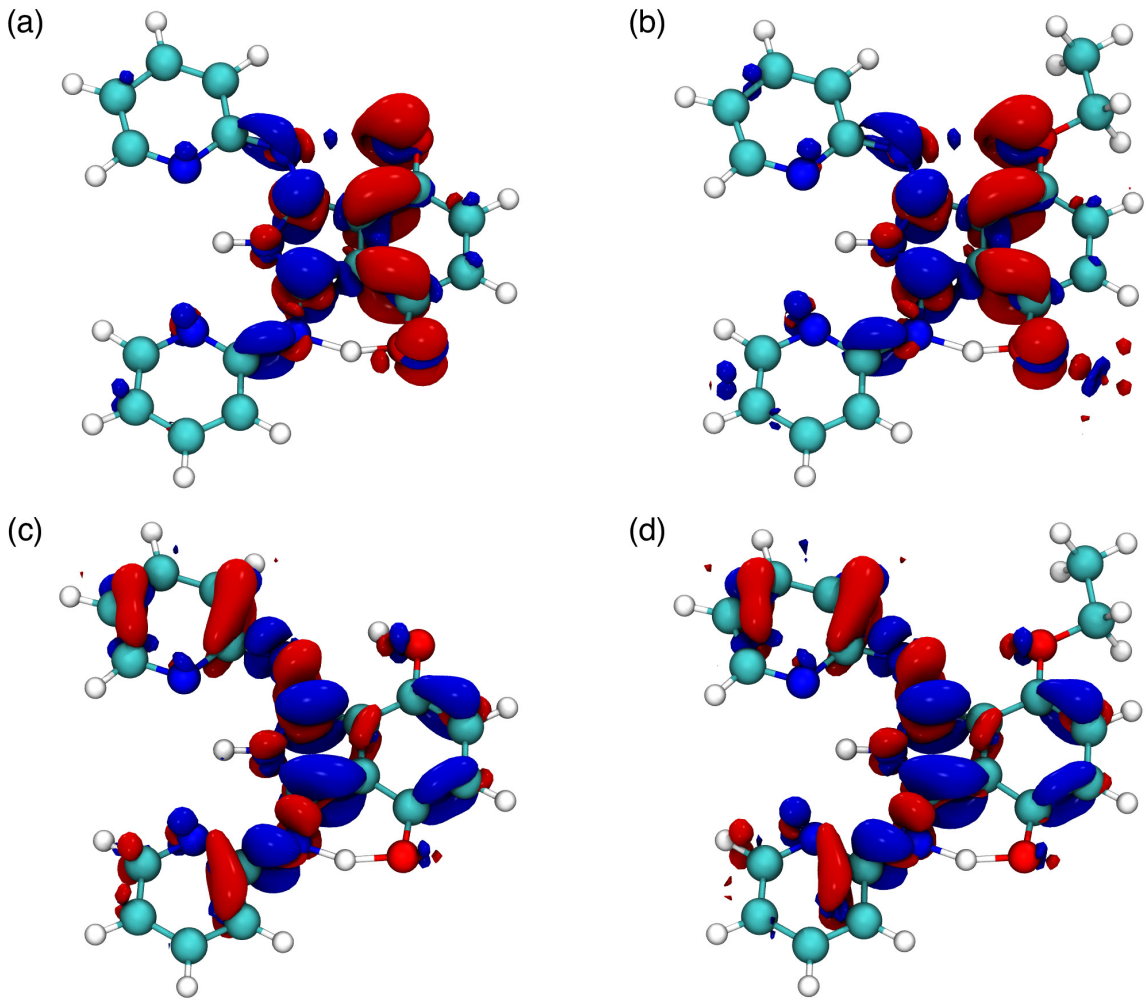

Figure S7: Electron density ρ differences between the ground state S_0 and the first and second excited states S_1 and S_2 at the transition state. Positive parts are shown in red and negative parts in blue. (a) Diol, $\rho_{S_0} - \rho_{S_1}$ (b) Ethoxy-ol, $\rho_{S_0} - \rho_{S_1}$ (c) Diol, $\rho_{S_0} - \rho_{S_2}$ (d) Ethoxy-ol, $\rho_{S_0} - \rho_{S_2}$.

this poses no problem to the present analysis, as we assume thermalization of the reactants on the S_1 state, which is consistent with either (i) excitation to S_1 and thermalization or (ii) excitation to S_2, rapid interconversion to S_1, and thermalization. Higher singlet states can be excluded as they are energetically inaccessible to excitation in the experiment, and triplet states can be excluded on the basis of the experimentally measured excited-state lifetimes and high quantum yields.[S1]

c. Robustness tests for the TD-DFT calculations

Three commonly employed exchange-correlation functionals (B3LYP,[S12,S13] CAM-B3LYP,[S14] M062X[S15]) are employed for the TD-DFT calculations reported in this study. The use of range of different functionals is worthwhile in this study, as excitations involving charge-transfer character are known to be problematic for TD-DFT calculations;[S19–S21] the employed functionals vary with regard to the amount of exact exchange included and with regard to long-range correction of the Coulomb interactions. Tab. S5 presents the barrier heights and relevant vibrational frequencies calculated using the three different functionals with the 6-31++G(d)[S18] basis set. For the various functionals, the barrier heights are generally consistent with each other to within 1 kcal/mol. The frequency of the unstable mode at the transition state is considerably lower for CAM-B3LYP, in accordance with the reduced barrier height obtained using this functional. The difference in the vibrational frequencies of the reaction coordinate are within 5 %. Although these barrier heights are relatively low, raising the possibility of non-equilibrium effects in the ESIPT dynamics, it is assumed in this study that semi-classical TST is applicable in this regime.

Table S5: The barrier height for the ESIPT reaction ΔV (in kcal/mol), imaginary frequency $\omega_1^\ddagger$ (in cm^{-1}) at the transition state, and frequency (in cm^{-1}) of the OH stretch for the reactant ω_1^r in the first excited state of the diol and the ethoxy-ol using TD-DFT with the 6-31++G(d) basis set and three different exchange-correlation functionals.

6-31++G(d)	ΔV in kcal/mol		$\omega_1^\ddagger$ in cm^{-1}		ω_1^rcm^{-1}	
Functional	Diol	Ethoxy-ol	Diol	Ethoxy-ol	Diol	Ethoxy-ol
B3LYP	5.9	4.8	1375	1260	3188	2966
M062X	5.9	4.7	1378	1264	3297	3075
CAM-B3LYP	5.1	3.7	1305	1126	3178	2909

Tab. S6 presents robustness tests of the barrier heights and vibrational frequencies with respect to the basis set (TZVP[S16,S17] and 6-31++G(d)[S18]) employed in the TD-DFT calculations. Again, barrier height differences are within 1 kcal/mol. The frequencies of the instable modes at the transition states are slightly lower with the TZVP basis set, which is

consistent with the decreased barrier heights obtained with this basis. The frequencies of the OH stretching modes at the reactant minimum differ by less than 2%.

Table S6: The barrier height for the ESIPT reaction ΔV (in kcal/mol), imaginary frequency $\omega_1^\ddagger$ (in cm^{-1}) at the transition state, and frequency (in cm^{-1}) of the OH stretch for the reactant ω_1^r in the first excited state of the diol and the ethoxy-ol using TD-DFT with the B3LYP exchange-correlation functional and two different basis sets.

B3LYP	ΔV in kcal/mol		$\omega_1^\ddagger$ in cm^{-1}		ω_1^r in cm^{-1}	
Basis set	Diol	Ethoxy-ol	Diol	Ethoxy-ol	Diol	Ethoxy-ol
TZVP	5.4	4.3	1277	1153	3195	2910
6-31++G(d)	5.9	4.8	1375	1260	3188	2966

Tab. S7 presents structural parameters related to the seesaw effect calculated using different exchange-correlation functionals and basis sets. Only very small deviations are found for these parameters demonstrating again the robustness of the calculations with respect to the exchange-correlation functional and basis set employed.

Table S7: Structural parameters on the first excited state S_1 related to the seesaw effect for the diol and ethoxy-ol obtained using using TD-DFT with different exchange-correlation functional and basis sets. For the definition of d, a_1 and a_2 see Fig. 1 in the main text. Distances given in Ångström.

	Diol			Ethoxy-ol		
	d	a_1	a_2	d	a_1	a_2
B3LYP/TVZP	1.96	130°	130°	1.79	127°	135°
B3LYP/6-31++G(d)	1.97	131°	131°	1.82	127°	135°
M062X/6-31++G(d)	1.98	130°	130°	1.84	127°	137°
CAM-B3LYP/6-31++G(d)	1.94	130°	130°	1.78	127°	134°

The robustness of the KIE and relative KIE with respect to the exchange-correlation functionals and basis sets employed is investigated next. To this end, the KIE is split up in three factors:

$$\mathrm{KIE} = \frac{k_\mathrm{H}(T)}{k_\mathrm{D}(T)} = \underbrace{\frac{\kappa_\mathrm{H}}{\kappa_\mathrm{D}}}_{\mathrm{KIE}_1} \cdot \underbrace{\frac{Q^\mathrm{r}_{D,\mathrm{vib},1}}{Q^\mathrm{r}_{H,\mathrm{vib},1}}}_{\mathrm{KIE}_2} \cdot \underbrace{\prod_{i=2}^{F} \frac{Q^\ddagger_{H,\mathrm{vib},i} Q^\mathrm{r}_{D,\mathrm{vib},i}}{Q^\mathrm{r}_{H,\mathrm{vib},i} Q^\ddagger_{D,\mathrm{vib},i}}}_{\mathrm{KIE}_3}. \tag{4}$$

We now demonstrate that the first of these terms, KIE_1, leads to the dominant source of exchange-correlation functional dependence that is seen for the KIE values in Fig. 4 of the main text. Fig. S8a reproduces the data for the full KIE values in Fig. 4 of the main text, and Figs. S8b-d present the corresponding results associated with each of the terms on the RHS of Eq. 4 above. It is clear from Fig. S8 that the dominant source of functional dependence emerges from the KIE_1 term, due to its dependence on the ESIPT barrier height.

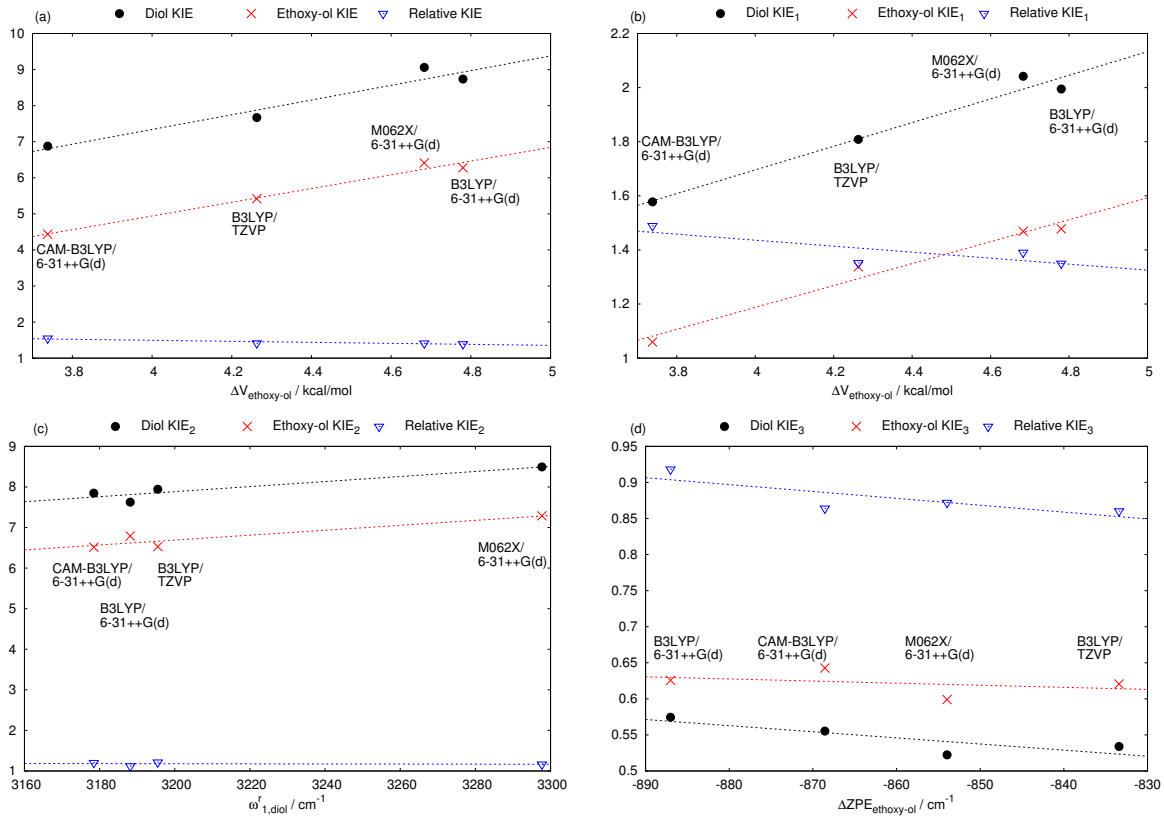

Figure S8: Scaling of the KIE in the diol (black) and the ethoxy-ol (red) and for their relative value (cyan) with respect to different exchange-correlation functionals and basis sets. Panel a: Full KIE, Panel b: First factor of Eq. 4 Panel c: Second factor of Eq. 4 Panel d: Third factor of Eq. 4.

Finally, an additional point of comparison between theory and experiment is provided via the vertical excitation energies (VEE) and Stokes shifts for the diol and ethoxy-ol. Tab. S8 provides these results for the full range of functionals and basis sets considered. Reasonable agreement between theory and experiment is found, with M062X and CAM-B3LYP performing well for these systems. As expected for an excitation with charge transfer character,

excitation and emission energies are underestimated when the B3LYP exchange-correlation functional is employed.[S22–S24] The seemingly better agreement for the LR PCM model than the SS PCM for the B3LYP functional is likely due to error cancelation of the well-known charge-transfer overstabilization in the B3LYP functional and the missing description of polarization effects in the LR PCM model, as has been previously emphasized.[S25]

Table S8: Excitation energies, emission energies and Stokes shifts for the diol and ethoxy-ol. If not specified, the basis set employed is 6-31++G(d).

	Diol			Ethoxy-ol		
	Excitation*	Emission†	Stokes‡	Excitation*	Emission†	Stokes‡
B3LYP/TZVP, LR	429	591	6390	434	606	6540
B3LYP/TZVP, SS	418	563	6144	436	577	5626
B3LYP, LR	432	592	6256	437	606	6382
B3LYP, SS	420	562	5979	438	575	5445
M06-2X, LR	362	550	9442	362	558	9703
M06-2X, SS	354	518	8992	363	530	8646
CAM-B3LYP, LR	366	546	9007	367	554	9197
CAM-B3LYP, SS	357	515	8627	368	526	8182
Experiment	387	596	9061	387	611	9473

* Excitation energies (in nm) from the reactant minimum on the ground electronic state to the first excited state, employing a non-equilibrium PCM.
† Emission energies (in nm) from the product minimum on the first excited electronic state (corresponding to a single proton transfer) to the ground electronic state, employing a non-equilibrium PCM.
‡ Units of cm^{-1}.

d. Experimentally implied ESIPT barrier heights

In general, the calculated ESIPT transfer times in Tab. 3 of the main text are significantly larger than those observed experimentally. The results in Fig. S9 present a rough estimate for the ESIPT barrier height that is implied by the experimental transfer times. The solid black circles reproduce the data in Fig. 3 from the main text. For each functional, we additionally present the experimentally implied barrier height that is obtained by fitting the experimental transfer time to the theoretically predicted transfer time, keeping all parameters in the rate calculation fixed except for the barrier height. The experimental results imply somewhat lower barrier heights (approximately 1.5 kcal/mol lower) than are obtained by

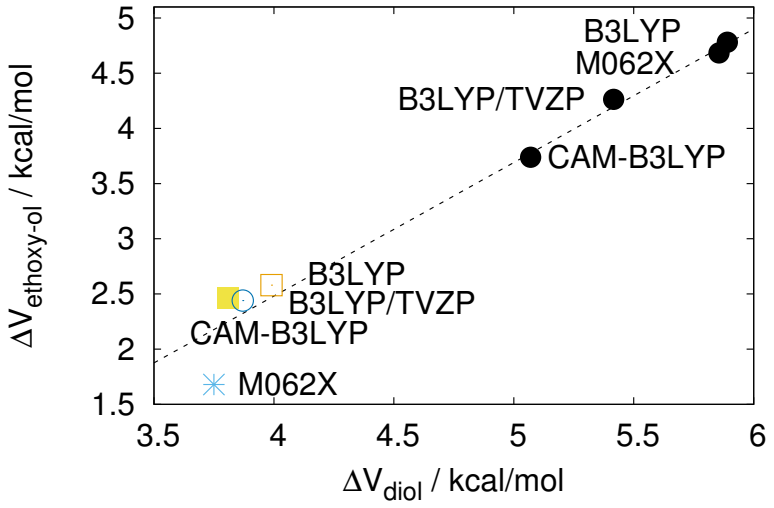

Figure S9: Experimentally implied ESIPT barrier heights (in kcal/mol) obtained for employing different exchange-correlation functionals and basis sets are shown as colored symbols (see text for details). The black circles reproduce Fig. 3 from the main text.

direct calculation, and we again note that these relatively low barrier heights for the reaction raise the possibility of non-equilibrium dynamical effects that are deferred for future study. Nonetheless, given that our experimentally-implied estimates of the reaction barriers are approximately 2.5 kcal/mol for ethoxy-ol and even higher for diol (see Fig. S9), which corresponds to approximately 4 kT at room temperature, it appears that TST is a reasonable starting point for analyzing the observed effects.

e. Comparison of the ethoxy-ol conformers

Fig. S10 shows the two different ethoxy-ol conformers (gauche and anti conformation) discussed in the main text.

f. Seesaw effect in the ground electronic state

The molecular seesaw effect discussed in the main text for the excited electronic state S_1 is also found for the ground state of both the diol and the ethoxy-ol. Optimized geometries and relevant bond distances and angles are given in Fig. S11 and Tab. S9.

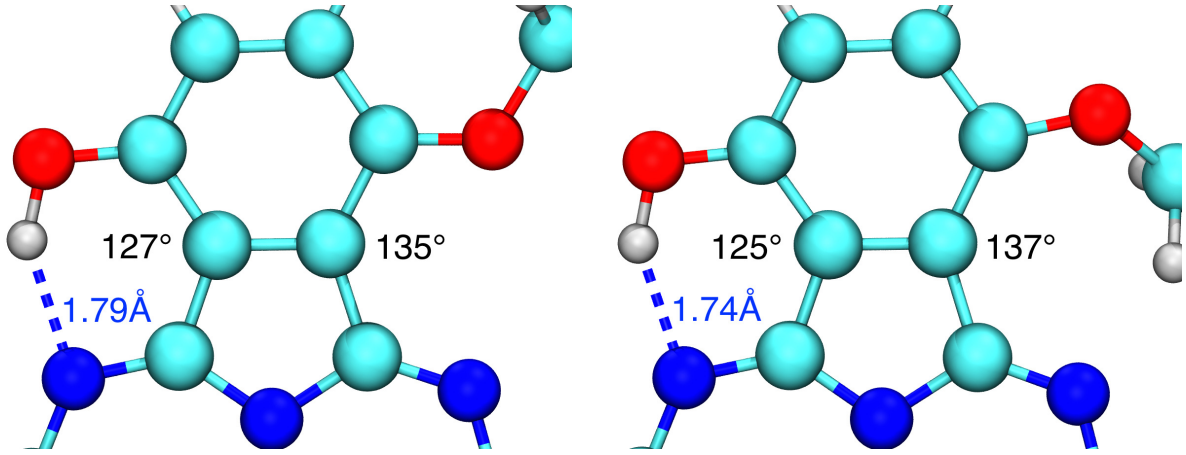

Figure S10: Anti (left) and gauche (right) conformations of the ethoxy-ol for the reactant in the S_1 state, along with along with important structural parameters. Distances are shown in blue and given in Ångström. Angles are shown in black.

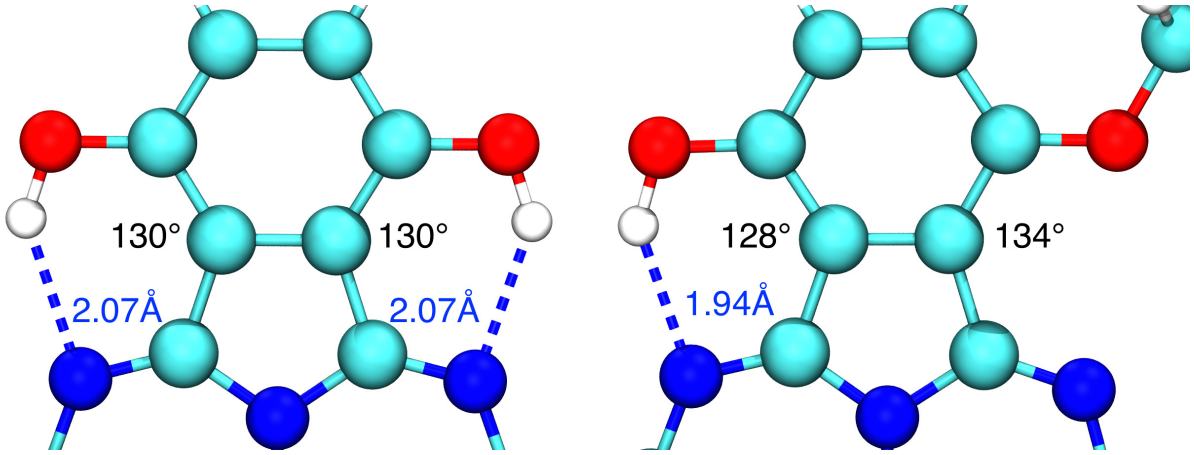

Figure S11: Depiction of the molecular seesaw effect in the ground state of the systems. Optimized geometries for the ESIPT reactant for the diol (left) and the ethoxy-ol (right) are shown from calculations at the B3LYP/TZVP level of theory. ESIPT distances are shown in blue and given in Ångström, and the C-C-C bond angles are shown in black.

Table S9: Structural parameters on the ground state related to the seesaw effect for the diol, ethoxy-ol, and methyl-ol obtained using B3LYP/TZVP. For the definition of d, a_1 and a_2, see Fig. 1 of the main text. Distances given in Ångström.

R	d	a_1	a_2
OEt-ap	1.94	128°	134°
OEt-sc	1.94	127°	134°
CH_3	1.95	128°	133°
OH	2.07	130°	130°

References

(S1) Hanson, K.; Patel, N.; Whited, M. T.; Djurovich, P. I.; Thompson, M. E. Substituted 1,3-Bis(imino)isoindole Diols: A New Class of Proton Transfer Dyes. *Org. Lett.* **2011**, *13*, 1598–1601.

(S2) Driscoll, E.; Sorenson, S.; Dawlaty, J. M. Ultrafast Intramolecular Electron and Proton Transfer in Bis(imino)isoindole Derivatives. *J. Phys. Chem. A* **2015**, *119*, 5618–5625.

(S3) Schrager, R. I.; Hendler, R. W. Titration of Individual Components in a Mixture with Resolution of Difference Spectra , pKs , and Redox Transitions. *Analyt. Chem.* **1982**, *54*, 1147–1152.

(S4) Fermann, J. T.; Auerbach, S. Modeling Proton Mobility in Acidic Zeolite Clusters: II. Room Temperature Tunneling Effects from Semiclassical Rate Theory. *J. Chem. Phys.* **2000**, *112*, 6787–6794.

(S5) Frisch, M. J.; Trucks, G. W.; Schlegel, H. B.; Scuseria, G. E.; Robb, M. A.; Cheeseman, J. R.; Scalmani, G.; Barone, V.; Mennucci, B.; Petersson, G. A.; Nakatsuji, H.; Caricato, M.; Li, X.; Hratchian, H. P.; Izmaylov, A. F.; Bloino, J.; Zheng, G.; Sonnenberg, J. L.; Hada, M.; Ehara, M.; Toyota, K.; Fukuda, R.; Hasegawa, J.; Ishida, M.; Nakajima, T.; Honda, Y.; Kitao, O.; Nakai, H.; Vreven, T.; Montgomery, J. A., Jr.; Peralta, J. E.; Ogliaro, F.; Bearpark, M.; Heyd, J. J.; Brothers, E.; Kudin, K. N.; Staroverov, V. N.; Kobayashi, R.; Normand, J.; Raghavachari, K.; Rendell, A.; Burant, J. C.; Iyengar, S. S.; Tomasi, J.; Cossi, M.; Rega, N.; Millam, J. M.; Klene, M.; Knox, J. E.; Cross, J. B.; Bakken, V.; Adamo, C.; Jaramillo, J.; Gomperts, R.; Stratmann, R. E.; Yazyev, O.; Austin, A. J.; Cammi, R.; Pomelli, C.; Ochterski, J. W.; Martin, R. L.; Morokuma, K.; Zakrzewski, V. G.; Voth, G. A.; Salvador, P.; Dannenberg, J. J.; Dapprich, S.; Daniels, A. D.; Farkas, .; Foresman, J. B.; Ortiz, J. V.;

Cioslowski, J.; Fox, D. J. Gaussian09 Revision E.01. Gaussian Inc. Wallingford CT 2009.

(S6) Tomasi, J.; Mennucci, B.; Cammi, R. Quantum Mechanical Continuum Solvation Models. *Chem. Rev.* **2005**, *105*, 2999–3094.

(S7) Li, X.; Frisch, M. J. Energy-Represented Direct Inversion in the Iterative Subspace within a Hybrid Geometry Optimization Method. *J. Chem. Theo. Comp.* **2006**, *2*, 835–839.

(S8) Peng, C.; Bernhard Schlegel, H. Combining Synchronous Transit and Quasi-Newton Methods to Find Transition States. *Israel J. Chem.* **1993**, *33*, 449–454.

(S9) Peng, C.; Ayala, P. Y.; Schlegel, H. B.; Frisch, M. J. Using Redundant Internal Coordinates to Optimize Equilibrium Geometries and Transition States. *J. Comp. Chem.* **1996**, *17*, 49–56.

(S10) Improta, R.; Barone, V.; Scalmani, G.; Frisch, M. J. A State-Specific Polarizable Continuum Model Time Dependent Density Functional Theory Method for Excited State Calculations in Solution. *J. Chem. Phys.* **2006**, *125*, 054103.

(S11) Improta, R.; Scalmani, G.; Frisch, M. J.; Barone, V. Toward Effective and Reliable Fluorescence Energies in Solution by a New State Specific Polarizable Continuum Model Time Dependent Density Functional Theory Approach. *J. Chem. Phys.* **2007**, *127*, 074504.

(S12) Lee, C.; Yang, W.; Parr, R. G. Development of the Colle-Salvetti Correlation-Energy Formula into a Functional of the Electron Density. *Phys. Rev. B* **1988**, *37*, 785.

(S13) Becke, A. D. Density-Functional Thermochemistry. III. The Role of Exact Exchange. *J. Chem. Phys.* **1993**, *98*, 5648–5652.

(S14) Yanai, T.; Tew, D. P.; Handy, N. C. A New Hybrid Exchange–Correlation Functional Using the Coulomb-Attenuating Method (CAM-B3LYP). *Chem. Phys. Lett.* **2004**, *393*, 51–57.

(S15) Zhao, Y.; Truhlar, D. G. The M06 Suite of Density Functionals for Main Group Thermochemistry, Thermochemical Kinetics, Noncovalent Interactions, Excited States, and Transition Elements: Two New Functionals and Systematic Testing of Four M06-Class Functionals and 12 Other Functionals. *Theo. Chem. Acc.* **2008**, *120*, 215–241.

(S16) Schäfer, A.; Horn, H.; Ahlrichs, R. Fully Optimized Contracted Gaussian Basis Sets for Atoms Li to Kr. *J. Chem. Phys.* **1992**, *97*, 2571–2577.

(S17) Schäfer, A.; Huber, C.; Ahlrichs, R. Fully Optimized Contracted Gaussian Basis Sets of Triple Zeta Valence Quality for Atoms Li to Kr. *J. Chem. Phys.* **1994**, *100*, 5829–5835.

(S18) Dill, J. D.; Pople, J. A. Self-Consistent Molecular Orbital Methods. XV. Extended Gaussian-type Basis Sets for Lithium, Beryllium, and Boron. *J. Chem. Phys.* **1975**, *62*, 2921–2923.

(S19) Jacquemin, D.; Perpete, E. A.; Scuseria, G. E.; Ciofini, I.; Adamo, C. TD-DFT Performance for the Visible Absorption Spectra of Organic Dyes: Conventional versus Long-Range Hybrids. *J. Chem. Theo. Comp.* **2008**, *4*, 123–135.

(S20) Casida, M.; Huix-Rotllant, M. Progress in Time-Dependent Density-Functional Theory. *Ann. Rev. Phys. Chem.* **2012**, *63*, 287–323.

(S21) Eriksen, J. J.; Sauer, S. P.; Mikkelsen, K. V.; Christiansen, O.; Jensen, H. J. A.; Kongsted, J. Failures of TDDFT in Describing the Lowest Intramolecular Charge-Transfer Excitation in Para-Nitroaniline. *Mol. Phys.* **2013**, *111*, 1235–1248.

(S22) Tozer, D. J.; Amos, R. D.; Handy, N. C.; Roos, B. O.; Serrano-ANDRES, L. Does Density Functional Theory Contribute to the Understanding of Excited States of Unsaturated Organic Compounds? *Mol. Phys.* **1999**, *97*, 859–868.

(S23) Dreuw, A.; Weisman, J. L.; Head-Gordon, M. Long-range Charge-Transfer Excited States in Time-Dependent Density Functional Theory Require Non-Local Exchange. *J. Chem. Phys.* **2003**, *119*, 2943–2946.

(S24) Bernasconi, L.; Sprik, M.; Hutter, J. Time Dependent Density Functional Theory Study of Charge-Transfer and Intramolecular Electronic Excitations in AcetoneWater Systems. *J. Chem. Phys.* **2003**, *119*, 12417–12431.

(S25) Guido, C. A.; Jacquemin, D.; Adamo, C.; Mennucci, B. Electronic Excitations in Solution: The Interplay Between State Specific Approaches and a Time-Dependent Density Functional Theory Description. *J. Chem. Theo. Comp.* **2015**, *11*, 5782–5790.